Hindawi
Advances in Materials Science and Engineering
Volume 2022, Article ID 2838691, 21 pages
https://doi.org/10.1155/2022/2838691

Research Article

Study and Numerical Analysis on Seismic Performance of Concrete *U*-Shaped Shear Wall

Jiuyang Li,[1] **Li Chen**,[1] **Xiaoyu Wang**,[1] **and Fangqi Li**[2]

[1]*School of Civil Engineering, Changchun Institute of Technology, Changchun 130012, China*
[2]*School of Landscape Architecture and Architecture, Shangqiu University, Shangqiu 476000, China*

Correspondence should be addressed to Xiaoyu Wang; 1241957603@qq.com

Received 27 May 2022; Revised 19 October 2022; Accepted 9 December 2022; Published 28 December 2022

Academic Editor: Shengwen Tang

Rectangular, *L*-shaped, and *T*-shaped section concrete shear walls in high-rise buildings are more frequently used in engineering and are widely studied. However, there are few studies related to the load-bearing performance of concrete shear walls with *U*-shaped sections. In this article, the seismic performance and damage mechanisms are analyzed in a systematic manner. In addition, a finite element model was developed using ABAQUS software, and numerical simulation was carried out. The damage forms and load-carrying capacity of shear walls with *U*-shaped sections were validated. Finally, reasonable suggestions and construction measures are given for the design of shear walls with *U*-shaped sections, and a benchmark is provided for relevant engineering applications.

1. Introduction

With the rapid development of multi-high-rise housing, people's requirements for an indoor space layout are gradually increasing. Conventional rectangular section force components, such as exposed columns and exposed beams, occupy building space and functionally fail to meet users' requirements [1–3]. Therefore, in order to overcome this issue, the vertical force components of high-rise residential buildings combined with the characteristics of frame columns and shear walls can form shear walls with *T*-shaped, *L*-shaped, cross-shaped, and *U*-shaped cross-sections [4, 5]. In Chile, the *T*-shaped, *L*-shaped, *C*-shaped, or *U*-shaped walls have been widely used with excellent performance, especially during severe earthquakes [6]. A concrete *U*-shaped cross-sectional shear wall can be arranged around the elevator, stairs, and other vertical components to make full use of the building area. The shear wall with a reasonable design of the wall limb section shows good stiffness, which can effectively resist winds, earthquakes, and other horizontal effects. Compared with the conventional rectangular section reinforced concrete shear wall, it can only provide one translational stiffness [7]. While the *U*-shaped cross-sectional shear wall can provide the stiffness needed for two translational directions of the structure and has excellent seismic performance, it is recognized that it has good marketing in both high-rise buildings and large space buildings.

Although the advantages of *U*-shaped cross-sectional walls are obvious, the application of *U*-shaped cross-sectional walls in engineering is still limited due to their unclear seismic performance, and few studies on the seismic performance of *U*-shaped cross-sectional walls have been observed. Beyer et al. [8] performed quasi-static cyclic tests on two *U*-shaped reinforced concrete walls, which provided a theoretical basis for studying the seismic performance of *U*-shaped walls and formulating appropriate design guidelines. Behrouzi et al. [7] tested three large *C*-shaped walls under unidirectional and bidirectional loads. It was found that the *C*-shaped wall has a symmetric response in the web direction and an asymmetric response in the flange direction. Constantin et al. [9] studied the quasi-static cyclic double load performance of two 1/2 scale reinforced concrete *U*-shaped cross-section walls along the diagonal direction of the *U*-shaped cross-section. Their results showed that: (1) the ductility of shear walls can be ensured by appropriately limiting the length of the free part of the flange;

(2) appropriately increasing the reinforcement of longitudinal reinforcement may delay or avoid excessive crushing of parts of concrete. Ile and Reynouard [10] studied the mechanical properties and performed a numerical simulation of a *U*-shaped cross-section wall under uniaxial and biaxial loads. It was concluded that the wall could withstand large bending and shear forces in both directions. However, no experimental study on the seismic performance of *U*-shaped cross-section walls under quasi-static loads in mutually perpendicular (along the *X*-axis and *Y*-axis directions in Figure 1) directions was observed.

Based on a local metro operation depot complex building project, this paper makes an in-depth study of the ultra-large *U*-shaped shear wall of the bottom floor. The first experimental study was carried out on shear walls under proposed static loads in two directions in order to analyze their seismic performance in terms of load-displacement response, ductility performance, stiffness degradation, and energy dissipation capacity. In addition, the respective roles and stress hysteresis effects of concrete and reinforcement in the hysteretic behaviour of shear walls are systematically analyzed. The reasons for the appearance of the pinching effect are revealed from a mechanistic point of view. Results showed that a good comprehensive performance evaluation of a *U*-shaped shear wall is obtained by comparing its seismic performance with that of rectangular, *T*-shaped, and *L*-shaped shear walls. The finite element nonlinear model of the shear wall was established and numerically analyzed using ABAQUS software, and the effectiveness of the simulation method was validated against the experimental results. The current study can provide a basis for seismic design, damage assessment, and strengthening of *U*-section shear walls in real applications. Moreover, it can also bring important theoretical significance and engineering value for further promoting the application of *U*-section shear walls.

2. Low Cycle Reciprocating Load Test of *U*-Shaped Section Shear Wall

2.1. Specimen Geometry Design. The construction site is located in Changchun city, northeast China. According to the seismic design code for buildings (GB50011-2010) [11], it shows that the local seismic intensity is 7 degrees (design basic seismic acceleration value 0.1 g), category *C* of defense (standard fortification 3 categories), design seismic grouping group I, and building site category II. The total building height is 54 m, seismic grade II, and the first floor is a subway operation depot with a building floor height of 9.0 m. 2–16 floors are residential, with a building floor height of 3 m. The schematic diagram of the first-floor structural layout is shown in Figure 2. Using PKPM [12] structural analysis software, the shear wall at the marked position is shown in Figure 2. The shear wall marked in Figure 2 was identified based on the maximum axial compression ratio being the most dangerous; the design axial force is $N = 13950$ kN and the axial compression ratio is 0.15; thus, the *U*-shaped section of concrete shear wall is determined as the research object.

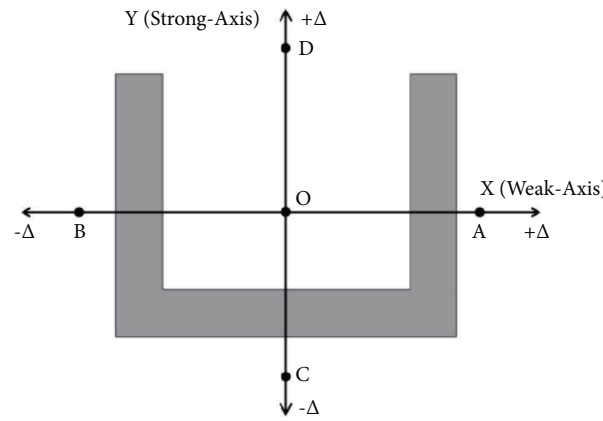

Figure 1: Loading direction diagram.

According to the principle of specimen scaling in the Theory and Technique of Engineering Structural Testing [14], the laboratory loading conditions were carefully considered, and the test specimens were finally determined to be made in a ratio of 1 : 5 for concrete shear walls with a *U*-shaped cross-section in accordance with the similarity of geometric proportions between the model and the original members. Also, the loads applied to the model were carried out strictly in accordance with the similarity of the original structural loads, and the relevant physical quantities during the model test were similar in certain proportions.

In the current study, in order to investigate the seismic performance of the shear wall with the *U*-shaped section subjected to forces in two directions, two reinforced concrete specimens were fabricated according to the loading directions (URC-X and URC-Y), and the bottoms of the specimens were cast together with the concrete base as a whole. The section of the shear wall is 870 mm × 730 mm × 120 mm (length × width × limb width), the height is 2000 mm, and the height of the base is 400 mm. The design parameters of the test model cross-section after scaling are illustrated in Figure 3 and Table 1. The specimens URC-X and URC-Y are loaded along the weak axis direction O ⟶ A ⟶ B ⟶ O and along the strong axis direction O ⟶ D ⟶ C ⟶ O, respectively. The schematic diagram of the loading direction is shown in Figure 1.

2.2. Design of Test Piece Reinforcement. The design of the specimens is mainly based on the seismic design code for buildings (GB50011-2010) [11], the concrete structure design code (GB 50010-2010) [15], the technical regulations for concrete structures in high-rise buildings (JGJ 3-2010) [16], the technical regulations for concrete anisotropic column structures (JGJ 149-2017) [17], and the relevant structural requirements and provisions for calculation and verification. The designed concrete grade of the shear wall is C30, and the concrete strength grade of the base is C35. According to the reinforcement of the prototype, the reinforcement of the specimen is calculated in terms of the principle of equal reinforcement rate. The specimen is configured with 16 HRB400-grade reinforcements of 12 mm diameter for the

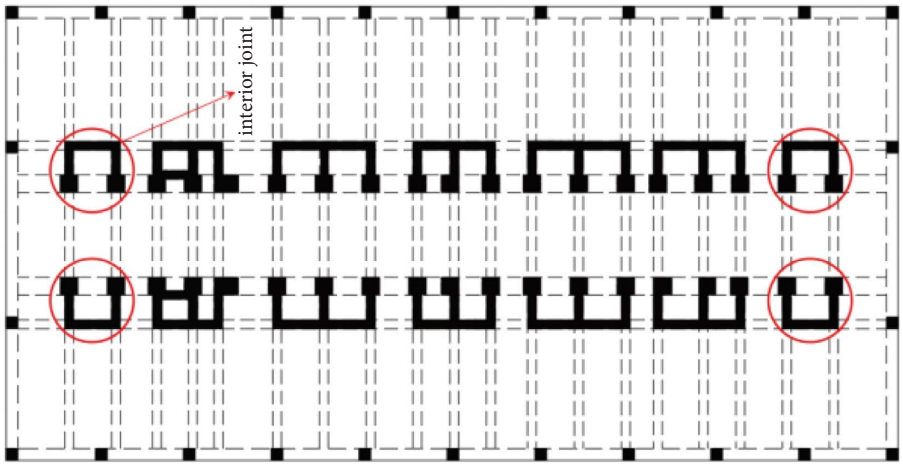

Figure 2: Architectural plan with a prototype *U*-shaped section wall.

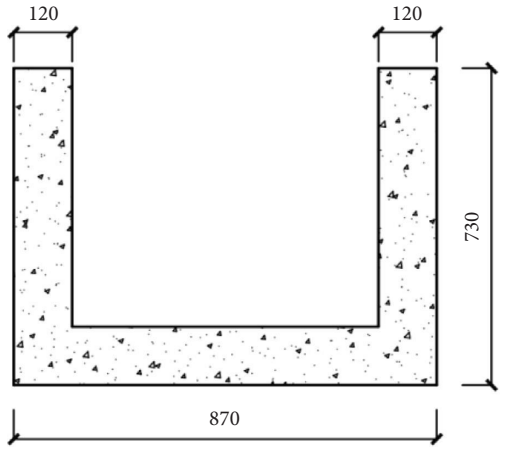

Figure 3: Model plane size drawing.

Table 1: Specimen design parameters.

Wall limb size (mm)	Web size (mm)	Overhang wing size (mm)	Stirrup	Horizontal tendon	Longitudinal bar	Overhanging wings longitudinal tendons
730 × 1600 × 160	870 × 1600 × 160	220 × 400 × 160	C6@150	C10@200	16C12 22C10 (1.41%)	12C10 (1.51%)

Note. C represents the strength grade of shear wall reinforcement.

restrained edge members and 10 mm for the other positions, and the spacing is 100 mm and 120 mm for the longitudinal reinforcement, respectively. The longitudinal reinforcement rate is 1.41%. The design parameters of the specimens (URC-X and URC-Y) are listed in Table 1 as well as shown in Figures 4 and 5.

In order to facilitate the lifting of the specimen and ensure the requirements of the fixed restraint at the root of the shear wall, a rectangular section base was designed with a base size of 1800 mm × 1500 mm × 400 mm, all of which were made of 26 HRB400 grade rebar with a diameter of 16 mm. During the test loading, the specimen base is connected to the laboratory loading special base plate by four ground bolts to meet the requirements of the fixed-end restraint at the bottom of the shear wall when the structure is subjected to horizontal thrust and an overturning moment. The base reinforcement diagram is shown in Figures 4 and 5. In order to prevent local damage at the loading end position, a 10 mm thick steel plate (with 2C12 anchor reinforcement) is designed, and the design details are shown in Figure 6.

2.3. Material Properties. C30 and C35 were used to pump commercial concrete for the members and foundation base, respectively, and manually vibrated. According to the requirements of the "Standard Test Methods for Mechanical Properties of Ordinary Concrete" and "Standard Test Methods for Concrete Structures" [18, 19], the compressive strength test was conducted on the six reserved concrete

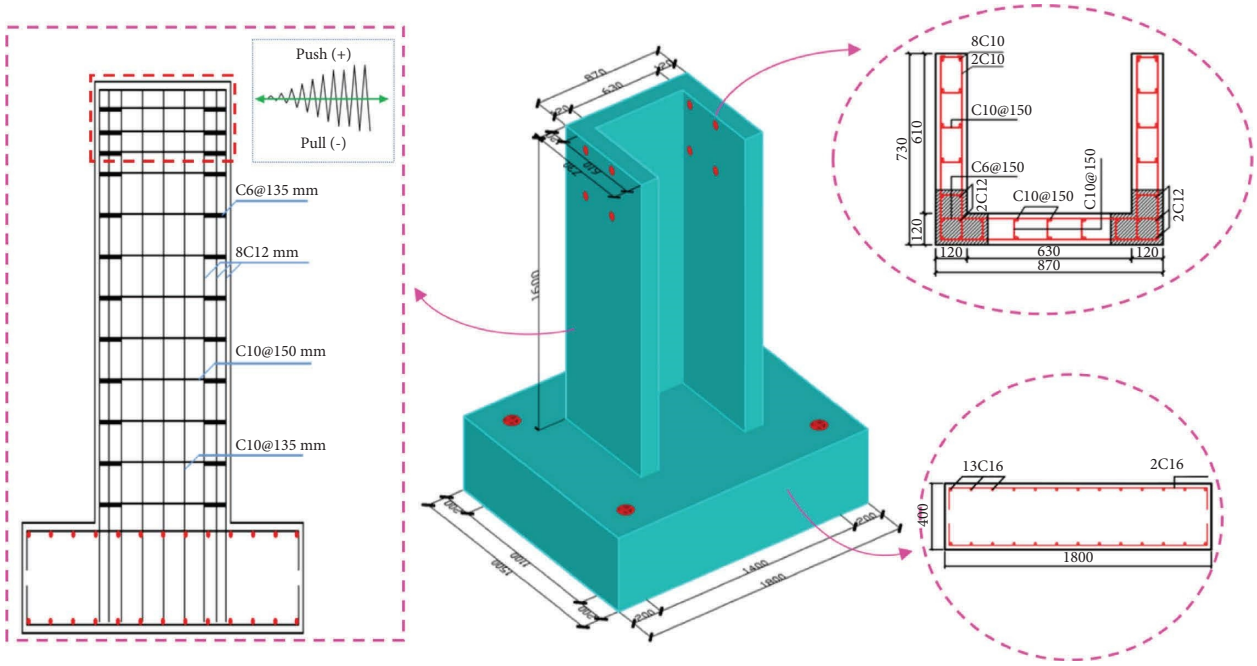

Figure 4: URC-X shear wall specimens and reinforcement diagram.

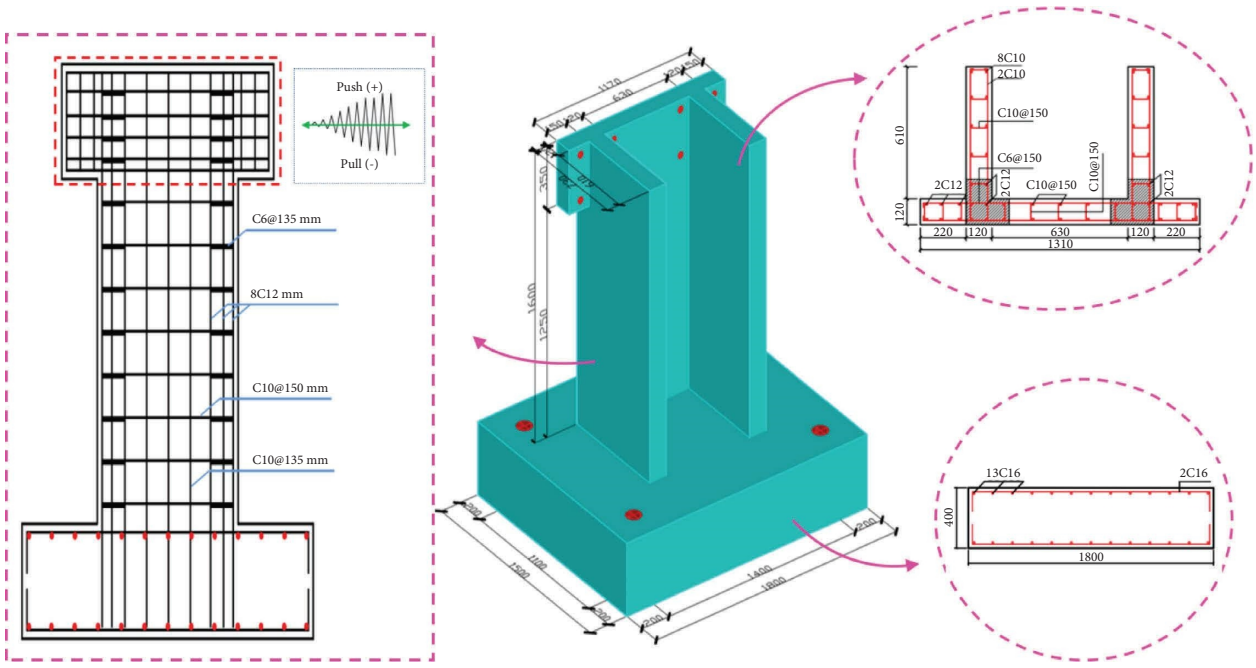

Figure 5: URC-Y shear wall specimens and reinforcement diagram.

cube specimens (100 mm × 100 mm × 100 mm). The 28-day compressive strength was 31.78 MPa (average 31, 31, 32, 31.5, 33, 32) and 31.75 MPa (average 31.5, 20.5, 29.5, 34.7, 34.2, 29.0).

The steel bar used in the specimen is HRB400. Material performance tests refer to the tensile tests of "metallic materials, Part 1: room temperature test method" (GB/T 228.1-2010) and "steel for reinforced concrete, Part 2: hot rolled ribbed bars" [20, 21]. Tensile tests were conducted with three specimens as a group. The average stress-strain curves and mechanical properties of the steel bars are shown in Figure 7 and Table 2.

2.4. Specimen Making. The specimens were constructed in two stages with concrete pouring. When pouring the foundation base, to fix the foundation base and the laboratory floor, the holes required for the anchor bolts are

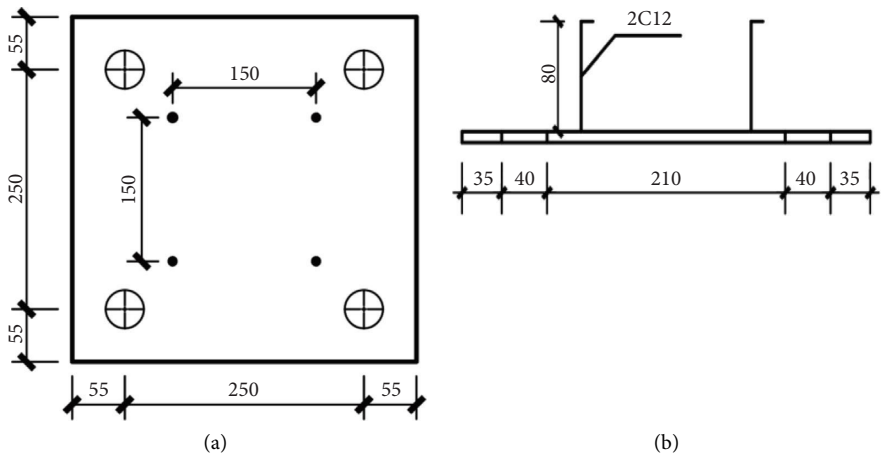

Figure 6: Steel plate design drawing. (a) Front view. (b) Side view.

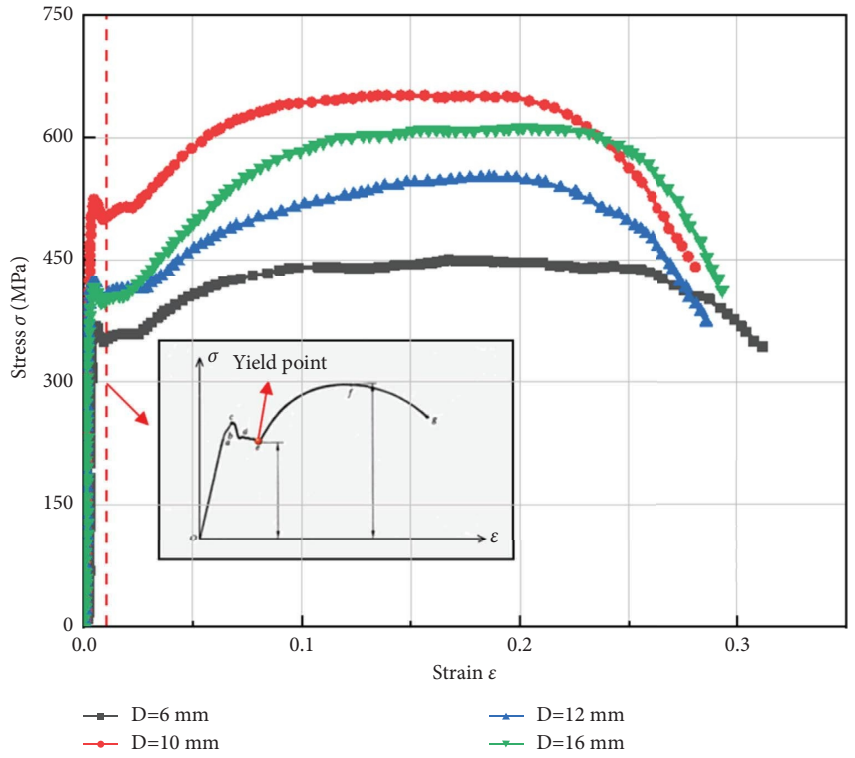

Figure 7: Average stress-strain curve.

Table 2: Mechanical properties of steel bars.

Category	Bar diameter (mm)	Specimen quantities	Yield strength (MPa)	Ultimate strength (MPa)	Elastic modulus (MPa)	Type
C (HRB400)	6	3	332	452	2.0×10^5	Ribbed
	10	3	550	646	2.0×10^5	Ribbed
	12	3	385	524	2.0×10^5	Ribbed
	16	3	464	622	2.0×10^5	Ribbed

reserved in the corners of the foundation base (Figure 8(a)). While loading, the foundation can be anchored on the laboratory ground through four anchor bolts with a diameter of 100 mm to make the lower fixed end of the shear wall rigid. The laboratory ground is smooth and rigid, and there is no need for a bottom mold during the

experiment. Plastic cloth is laid on the ground to prevent pollution and facilitate demolding. The side die is fixed with steel formwork and steel wire. Before the foundation base is poured, to ensure the spacing and location of longitudinal reinforcement, the shear wall longitudinal reinforcement is inserted into the foundation for anchoring. The horizontal anchorage length is 200 mm, and the vertical section is divided into two parts: 667 mm for half of the longitudinal bars and 1167 mm for the other half. Two plane thin wood plates with a thickness of 2-3 mm larger than the wall limb of the shear wall are designed. The holes are drilled into the wood plate according to the position of the shear wall's longitudinal reinforcement. The shear wall's longitudinal reinforcement passes through the corresponding holes in the wood plate and reaches the foundation. The longitudinal bars of the shear wall extend through the corresponding holes in the plank and into the foundation. The longitudinal bars are bent at 90 degrees at the bottom of the shear wall and welded to the base plate reinforcement to ensure the position of the longitudinal bars of the shear wall (Figure 8(b)). To facilitate hoisting, when the foundation base is poured, the built-in thread sleeve is embedded in the position of the lifting point calculated at the four corners of the base and was fixed by obliquely lapping steel bars (Figure 9(a)).

To ensure that the shear wall and the foundation base are integrated after pouring, the chiseling process is adopted at the connection between the wall limb and the base after the initial concrete solidification. (Figure 9(b)) When the foundation strength reaches 20 MPa ("Concrete structure engineering construction quality acceptance specification" GB 50204-2015) [22]. Welded connections are made to the longitudinal bars reserved for the base of the foundation using the same diameter and the same number of bars. Attaching reinforcement strain gauges (4 mm × 10 mm) at vertical bars and tying horizontal reinforcement. The resistance method was used to detect the adhesive quality of the strain gauge before and after concrete pouring, while the distribution position of the strain gauge was recorded (Figure 9(c)). To prevent local damage at the end of the loading position of the shear wall, we embedded parts in the wall of the symmetrical loading point. (Perforation is required for an indwelling screw on embedded parts). The fabrication of embedded parts is shown in Figure 9(d).

Support the "concave" shear wall formwork after the wall reinforcement is tied. Scaffolds are supported on the outside of the formwork, while tension bolts are used between the inside and outside of the wall limb formwork to ensure the stability of the formwork during concrete pouring (Figures 10(a) and 10(b)).

2.5. Loading Scheme

2.5.1. Loading Device. The test was carried out in the structural laboratory of Changchun College of Engineering to study the load-carrying capacity and seismic performance of concrete shear walls with *U*-shaped sections under the proposed static load. After the specimen has been maintained, lift it to the test location, using the foot bolt to fix the specimen and the base, and install the force application device, the rated thrust of 500 kN, stroke ±250 mm, TWD electro-hydraulic servo actuator fixed in the test chamber loading reaction wall, and reciprocal horizontal action to be applied to the specimen. The axial load of the specimen is 537.97 kN, calculated by the axial compression ratio $n = 0.15$, and the axial force of the specimen is 558 kN, calculated by the PKPM analysis of the maximum internal force according to the similar relationship. Taking the maximum vertical axial force of 558 kN produced by the YDT 3000–200T hydraulic cylinder with the rated load of 3000 kN, the action point is at the geometric center of the *U*-shaped section. The loading schematic for the two specimens is shown in Figure 11. The test equipment installation position is shown in Figure 12.

2.5.2. Loading System. The loading system adopts mixed force-displacement loading. Pre-loading is carried out prior to the test, which will mainly check whether the actuator, control system, and data acquisition system are working properly, as well as observe the state of the specimen's loading point and base. When the formal loading is started, the specimen is loaded with a cyclic load in steps of 1/5 of the yield load before yielding. When the specimen reaches yielding, then it will switch to displacement-controlled loading and be cycled twice according to the yield displacement value in each increment. When the load drops to 85% of the peak load, the specimen is damaged, and the test loading is stopped. The loading regime of the test is shown in Figure 13.

3. Test Procedure

During the test, both specimens experienced the elastic stage, crack stage, yield stage, continuous stage, and failure stage under the combined action of the reinforced skeleton and core concrete, with approximately the same test phenomena. The crack development process of the URC-X specimen is shown in Figure 14 and that of the URC-Y specimen in Figure 15.

3.1. Elastic Stage. When the load is small, the displacement increases linearly as the force increases; the pattern of change in the elastic phase is the same for both specimens, and the specimens are made without defects.

3.2. Crack Stage. Both specimens start with horizontal cracks in the wall limb at a certain height from the base surface. With the increase in load, the width of the horizontal crack increases and extends to the middle wall of the web, forming oblique cracks. This shows that the specimen first produces bending cracks, and then it is in the bending shear stress state.

(a) (b)

Figure 8: Manufacturing process of the base skeleton. (a) Base reinforcement skeleton. (b) Bottom supporting mold.

(a) (b)

(c) (d)

Figure 9: Template support for preliminary work. (a) Pre-embedded thread sleeve. (b) Chiseling the connection surface. (c) Detection strain gauge. (d) Making embedded parts.

(a) (b)

Figure 10: Fabrication and formation of walls. (a) Formwork support. (b) Specimen shaping.

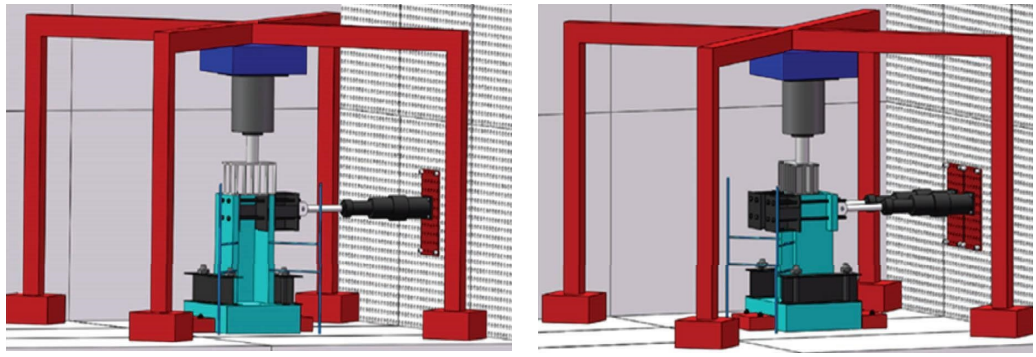

(a) (b)

Figure 11: Loading schematics of two specimens. (a) URC-X loading diagram. (b) URC-Y loading diagram.

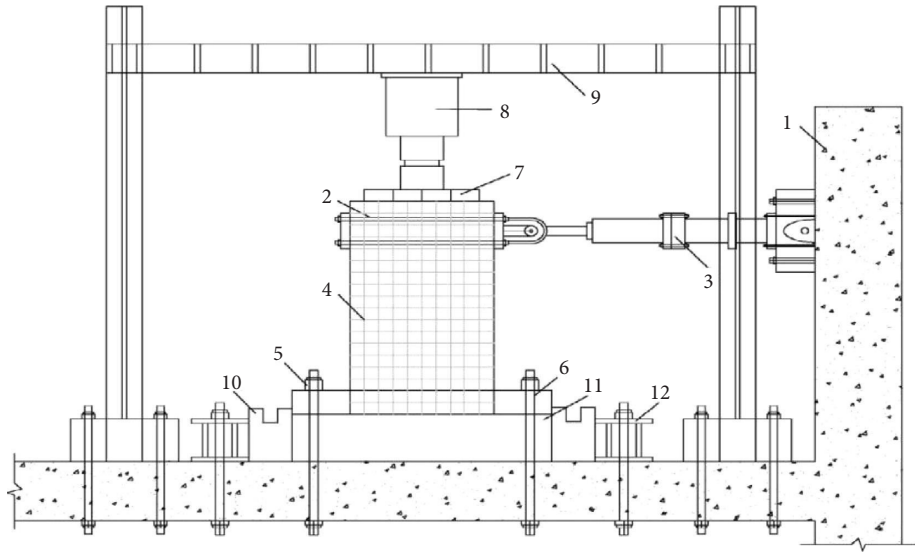

1.Reaction Wall 2.Guide screw 3.Loading cell 4.Shear Wall Specimen
5.High-strength bolt 6.Rolled Screw 7.Loadjing box beam 8.Hydraulic Jack
9.Reaction frame 10.Box girder 11.Footing of foundation 12.Rigidity Anchorage Beam

Figure 12: Arrangement of test devices and instrumentation devices.

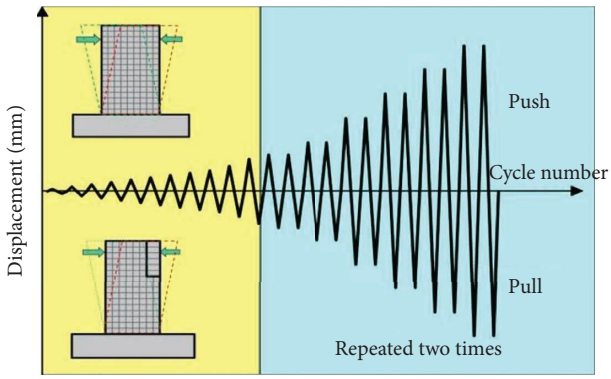

Figure 13: Loading protocol.

3.3. Yield Stage. When the horizontal load reaches the peak load, some horizontal cracks and oblique cracks appear in the wall limb 1, wall limb 2, and web, and the oblique cracks gradually develop in the upper part of the wall. At this time, the steel bars in the wall limbs yielded and there was a tendency for the concrete to spall.

3.4. Continuous Stage. After the horizontal load exceeds the peak load of the specimen, numerous oblique cracks appear at the interface between the wall limb and the web, and the cracks gradually expand to the upper part. Due to the reinforcement encrypted at the interface between the web and the wall limb, the stirrups and tie bars play a good constraint role, while the concrete at the interface is crushed but not obviously dropped. At the same time, the yield of reinforcement at the wall limb leads to the collapse phenomenon while the bearing capacity decreases gradually. However, the core area of the concrete will still maintain a good working state, thus reflecting that the URC specimen has good ductility and energy dissipation capacity.

(a) (b) (c)

Figure 14: Damage results of URC-X specimen. (a) Wall limb 1. (b) Web. (c) Wall limb 2.

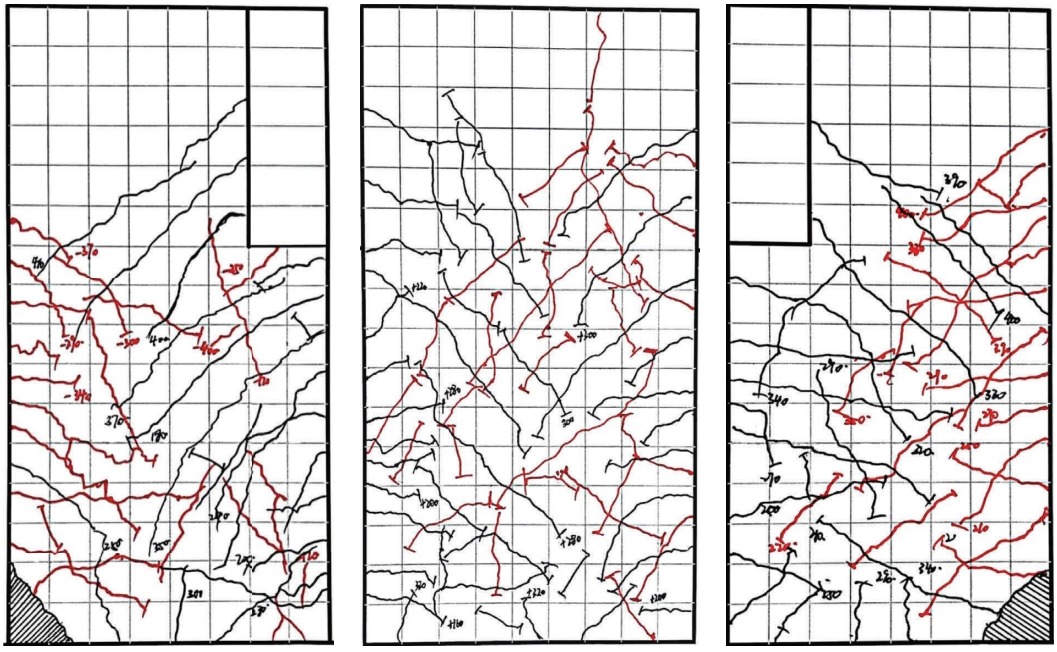

(a) (b) (c)

Figure 15: Damage results of URC-Y specimen. (a) Wall limb 1. (b) Web. (c) Wall limb 2.

3.5. Failure Stages. With the yield development of reinforcement at the bottom of the wall limb, the external concrete is completely crushed and fell. Inclined cracks penetrate the shear wall and form a "*V*" shape. However, the horizontal crack width of the web is obviously smaller than that of the wall limb. With the shear wall oblique cracks along the height of the wall distribution, there are more oblique cracks in the lower part, and the width is greater than the upper oblique cracks. The steel bars in the web generally yield to a certain extent, and the concrete peels off more.

Tables 3 and 4 show the test results for the URC-X specimen and URC-Y specimen, respectively.

Table 3: Experimental phenomena of URC-X.

P/Δ	Observed results
P = 0~160 kN	No obvious cracking of specimens
P = 160~200 kN	Horizontal cracks appear at the interface between the web and the wall limb, tending to develop downward-inclined cracks, and the shear wall is in the cracking stage
P = 200~230 kN	Wall limb 2 steel bars yield first under tension, and the specimen enters the yield stage
Δ = 10~30 mm	The horizontal cracks between the web and the wall limb gradually develop into oblique cracks with an inclination angle of 20°–60°.
Δ = 30~40 mm	The concrete at the bottom of wall limb 2 was slightly exfoliated, and the cracks at the bottom formed "*V*" and "*X*" shapes, and the crack width gradually increased. The distribution of cracks at the wall limb was dense at the abdomen and sparse at the end
Δ = 40~50 mm	Steel bar buckling at the junction of wall limb 1 and web, outward expansion, spalling of the external concrete protective layer, concrete crushing of the three-sided wall, a sharp drop of horizontal load, and specimen failure

Table 4: Experimental phenomena of URC-Y.

P/Δ	Observed results
P = 0~190 kN	No obvious cracking of specimens
P = 190~250 kN	Horizontal cracks appear at the bottom of wall limb 1 and wall limb 2, and the shear wall is in the cracking stage
P = 250~280 kN	The steel bars arranged in the wall limbs yield first and the yield stage begins
Δ = 10~30 mm	Horizontal cracks at the bottom of wall limbs and webs develop upward gradually and become oblique cracks
Δ = 30~50 mm	The original cracks in wall limb 1 and wall limb 2 become longer and wider and more oblique cracks appear in the middle and upper parts, and develop to the lower part, forming cross cracks. There are fewer new cracks, and the horizontal load reaches its peak.
Δ = 50~70 mm	The oblique crack of the web intersects with the horizontal crack to form the main crack; the web crack penetrates, the steel bar buckles, the bottom concrete falls off, and the wall limb does not judge the longitudinal reinforcement fracture

4. Analysis of Seismic Performance and Damage Mechanism under Cyclic Load

4.1. Load Displacement Hysteresis Curve and Skeleton Curve. The hysteresis curve is a load-displacement envelope formed by the applied horizontal loads and the corresponding displacements at each stage, which is used to reflect the seismic performance of shear walls under reciprocating loads. In order to better reflect the force and deformation characteristics of the specimen at each stage, the skeleton curve is obtained by connecting the peak load points of the first cycle in the hysteresis curve under each level of load [23].

4.1.1. Specimen URC-X. At the initial loading stage of the URC-X specimen, the hysteresis curve is a slender ring, showing a certain residual deformation and stiffness degradation. When the peak load reaches positive and negative values, the loading and unloading curves do not coincide, resulting in irreversible plastic deformation. After reaching the peak load, the hysteresis curve is closely extruded, the curve decreases rapidly, and the strength degradation is obvious. Figure 16 shows the skeleton curves in two different directions are not completely symmetrical, while the displacement is quite different, indicating that the positive hysteresis curve has a low bearing capacity and high ductility, and the negative hysteresis curve has a high bearing capacity and low ductility. The main reasons are as follows:

(1) Since the concave internal of the *U*-shaped shear wall is "hollow," to ensure the effective transmission of applied load between two wall limbs, a box-shaped steel beam with a large self-weight is placed between two wall limbs and suspended by a hook. Due to the steel beam absorbing energy, the positive and negative loads cannot act on two wall limbs equivalently.

(2) Under positive and negative cyclic loading, the *U*-shaped shear wall forces and transmits force through the wall limb. Compared with the web, a stress lag phenomenon was observed in the wall limbs, which cannot realize the overall joint force of the two wall limbs, resulting in the corresponding displacement hysteresis effect.

(3) Due to the construction error, the thickness of wall limb 1 is 100 mm larger than that of wall limb 2, in which the section height of wall limb 1 under positive load is large, which has a strong influence on the positive force.

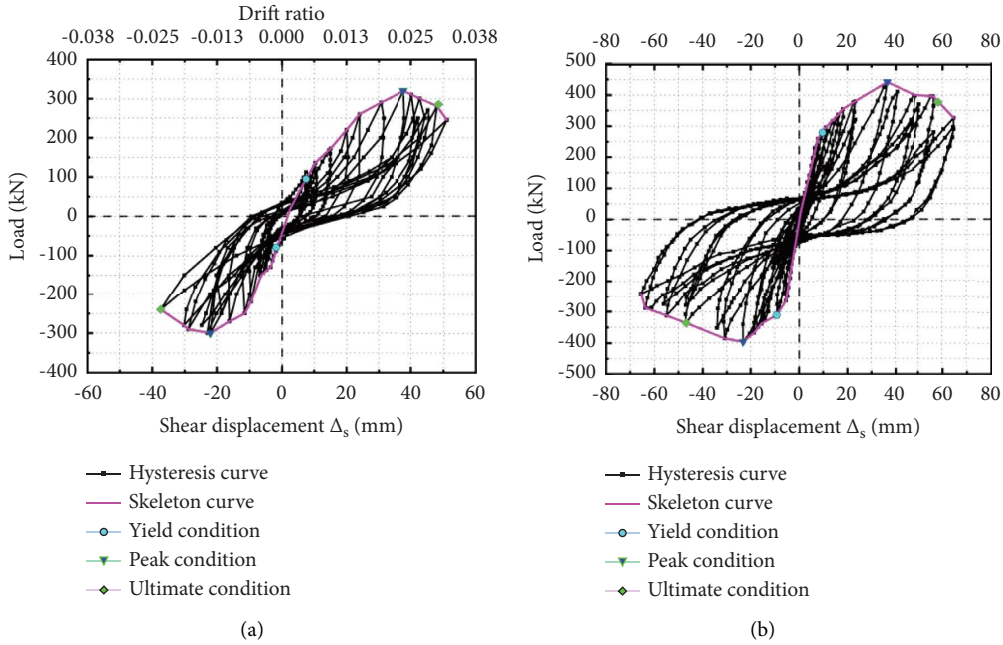

Figure 16: Hysteresis curve and skeleton curve. (a) URC-X. (b) URC-Y.

4.1.2. Specimen URC-Y. At the initial loading stage of the URC-Y specimen, the hysteresis curves of the specimen are all several straight lines with elastic characteristics, the closed area is small, and the stiffness degradation and residual deformation are small. With the concrete cracking, the horizontal displacement increases, and the stiffness of the curve gradually tends to 30 degrees. The hysteresis line and the surrounding area gradually increased, and internal damage gradually accumulated. When the peak load is reached, the hysteresis curve presents a compression phenomenon, mainly due to the gradual buckling of slightly exfoliated concrete and steel bars. When the peak load is reached, the hysteresis curve presents a compression phenomenon, mainly due to the gradual buckling of slightly exfoliated concrete and steel bars, the specimen presents a bending-shear failure, and the hysteresis curve develops into a bow shape with an obvious pinching effect. When the ultimate displacement is reached, the degradation of the hysteresis curve is obvious. When the lateral load is restored to zero, obvious residual deformation can also be seen. The hysteresis curve of the specimen during the whole loading process is fusiform. The load of the second cycle at the loading stage after the peak displacement is smaller than that of the first cycle. The curve decreases slowly, while the strength degradation is slow, thus showing certain ductility. The main reasons for the fusiform hysteretic curve are as follows: (1) the influence of cracked concrete on the hysteresis curve; (2) the influence of the steel bar pinching effect on the hysteresis curve; (3) the effect of hysteresis and the effect of reinforcement stress on the hysteresis curve. The specific effect mechanisms are analyzed as follows:

(1) The influence of cracked concrete on the hysteresis curve

With the increase in lateral displacement, the concrete enters nonlinear compression, which will remain an unrecoverable compression deformation. When the load reaches its peak and enters unloading, the compressive zone stresses in the concrete release, forming a nonstress tensile zone, and cracks appear again. The original tensile zone has residual compression deformation, which causes accumulation from repeated loading process, resulting in cracks that cannot be closed immediately. The crack at the end of the wall limb is reopened, while the crack in the web cannot be closed immediately, and the strength and stiffness of the component cannot be effectively restored. Only when the reverse displacement reaches a certain degree, the concrete tensile cracks are effectively closed. With the loading, the displacement required for the crack closure is increasing, resulting in the obvious pinching effect.

(2) The influence of the steel bar pinching effect on the hysteresis curve

Ideally, the hysteresis loops from tension to compression should be rhombic or a parallelogram [24]. In the compression state, the cracks in the concrete are closed. At this time, the concrete can be considered a continuum, while the deformation difference between steel and concrete is small. However, once the concrete enters tension, the main deformation is elastic strain, discontinuous behavior

occurs, and the reinforcement remains continuous without damage. In the process of a steel bar from tension to compression, the effect of the concrete is small, while the steel bar presents an ideal hysteresis state. When the steel bar is converted from compression to the beginning of tension, the deformation difference between concrete and steel bar is small, and the two are cooperatively stressed. The pressure provided by the concrete is greater than that of the steel bar. The compressive steel bar and the concrete bear the tensile force of the steel bar on one side, while the change speed is far less than that of the tensile steel bar on the other side, thus showing a slow growth arc curve.

(3) The effect of hysteresis and the effect of reinforcement stress on the hysteresis curve

As the specimen is subjected to reciprocal forces, when the load on the specimen changes from tension to thrust, accordingly, one side of the reinforcement goes from tension to compression, and the other side goes from compression to tension, while the time required for the conversion of the reinforcement from compression to tension and the conversion of the reinforcement from tension to compression is different. The steel bars on both sides of the center may be tensioned or compressed at a certain time, and the contribution of the bending moment will offset each other, in which the hysteresis curve of the steel bar becomes smooth [25].

4.2. Bearing Capacity and Deformation Capacity. In the current study, two *U*-shaped section specimens tested in this paper under the same coordinate system were ploted, as shown in Figure 17. The load and displacement parameters at the characteristic points of the specimens at each stage are listed in Table 5. The load and displacement of the specimen at yielding were determined by using the "*R* Park" method (cut-line stiffness method) [26]. The horizontal line of the maximum load value intersects with the origin and the $0.6P_{max}$ connection extension line. The intersection point between the vertical line of the intersection point and the curve is the yield characteristic point. When the peak load decreases by 15%, it is the corresponding limit displacement. In order to better analyze the deformation performance of shear walls, the introduction of a ductility coefficient [27] for analysis is shown in Table 5.

From Figure 17 and Table 5, we obtained the following:

(1) When loading along the *X*-axis direction (O-A-B-O shown in Figure 1), the peak load and ultimate bearing capacity of the specimen are low, and the deformation capacity is weak.

(2) When loading along the *Y* axis (O-D-C-O shown in Figure 1), the maximum bearing capacity may reach 458.16 kN, the ultimate displacement increases, the deformation capacity is good, and the member has good ductility.

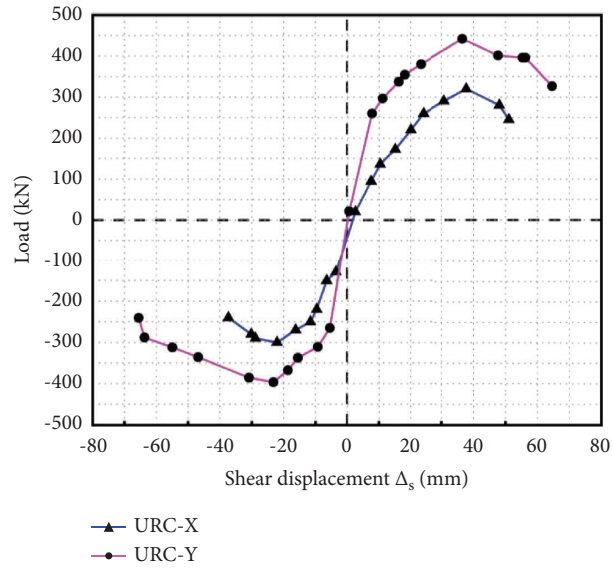

Figure 17: Comparison of skeleton curves of each specimen.

(3) According to the comparison of three main loads of URC-X and URC-Y, it shows that the bearing capacity of the *U*-shaped section shear wall on the strong axis is 34.71% higher than that on the weak axis, while the ductility increases by 39.42%.

4.3. Stiffness Degradation. Stiffness degradation is an important index in evaluating the seismic behavior of reinforced concrete structures. Cut-line stiffness K_i is the main index used to measure the stiffness degradation of specimens under cyclic loading [28]. The definition formula for "Code for Seismic Test of Buildings" in China [29] is as follows:

$$K_i = \frac{|+F_i| + |-F_i|}{|+\Delta_i| + |-\Delta_i|}, \quad (1)$$

where $+F_i$ and $-F_i$ are the load values of the positive and reverse peak points of the i cycle; the unit is kN. $+\Delta_i$ and $-\Delta_i$ are the deformation values of the forward and reverse peak points of the i cycle, and the unit is mm.

We used the same method for the comparative analysis of shear walls SW1, SWT, and SWL and the cut line stiffness of each specimen, as shown in Figure 18. During the loading process, the secant stiffness of the specimen presented a similar shape, which decreased with the increase in displacement. In the initial loading stage, due to cracks in the concrete; the secant stiffness of the specimen decreases rapidly. The gradual buckling of longitudinal reinforcement and the gradual widening of concrete cracks in the late loading stage has led to unstable changes in the plastic bearing capacity of members. The secant stiffness of the specimen gradually decreased and tended to be flat.

4.4. Energy Dissipation Capacity Analysis. Energy dissipation E reflects the energy dissipation of the specimen in a load cycle, which is expressed by the area of the hysteresis curve of

Table 5: Summary of comparison analysis results.

Specimen	P_y (kN)	Δ_y (mm)	P_{max} (kN)	Δ_{max} (mm)	P_u (kN)	Δ_u (mm)	μ
URC-X	292.66	20.04	340.12	37.82	250.70	48.37	2.41
URC-Y	360.16	19.19	458.16	36.56	371.00	64.56	3.36

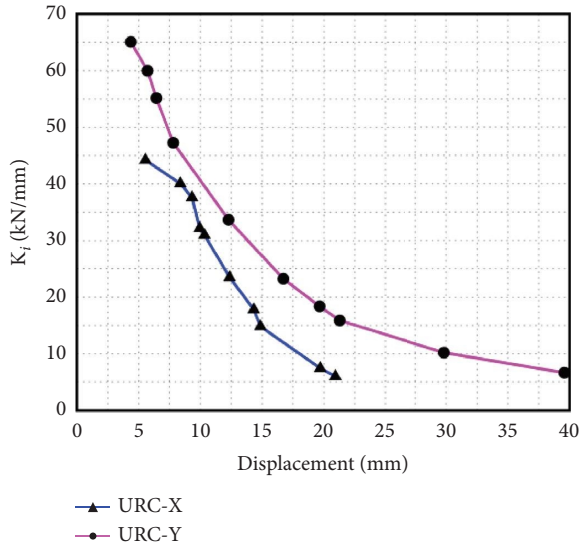

Figure 18: Overall stiffness degradation curve.

each cycle. The relative degree of absorbed energy of a shear wall is usually expressed by its equivalent damping coefficient [30]. The energy dissipation curve E and the equivalent damping coefficient ζ_{eq} of the specimen are shown in Figure 19. The area surrounded by the hysteresis loop is proportional to the equivalent damping coefficient. The energy dissipation coefficient E and equivalent damping coefficient are calculated as follows:

$$E = \frac{S_{ABE}}{S_{(OBC+OEF)}}, \qquad \zeta_{eq} = \frac{1}{2\pi}\frac{S_{ABE}}{S_{(OBC+OEF)}}, \tag{2}$$

where S_{ABE} represents the area enclosed by the hysteresis loop in Figure 20; $S_{(OBC+OEF)}$ represents the sum of the areas of triangles OBC and OEF in the figure.

Figure 19 shows that the energy dissipation and equivalent damping coefficients of specimens URC-X and URC-Y gradually increased with the increase in cyclic load. When the yield load is reached, the equivalent damping coefficient increases linearly to 0.05–0.08 and 0.09–0.12. When it is at its peak load, the equivalent damping coefficient of the specimen reaches around 0.20–0.22 and 0.23–0.29. It indicates that the specimen has good energy dissipation performance.

4.5. Strain Analysis. During the loading process of the test, the strain gauges of each longitudinal bar were alternated with various degrees of compressive and tensile states. Under low cyclic loading, the longitudinal reinforcement of the web appears as plastic compressive deformation and accumulates with the increase in load, which eventually leads to the buckling of the longitudinal reinforcement of the web. According to the actual material properties of steel bars (400 MPa), the longitudinal yield strain is 1800 $\mu\varepsilon$. From the test results, the strain of the longitudinal reinforcement of the specimen reached 2500 $\mu\varepsilon$, which indicates that the yield of the longitudinal reinforcement at the bottom of the specimen occurs during repeated loading.

5. Numerical Analysis

In order to eliminate various influencing factors from the tests, the group conducted numerical simulations using the finite element software ABAQUS/Standard, which has a library of various types of material models to simulate the properties of typical engineering materials, including metals, polymers, composites, reinforced concrete, and other materials [31–35]. ABAQUS has been widely used in civil engineering in recent years due to its powerful analytical capabilities and reliability in simulating complex structures.

5.1. Finite Element Analysis and Modeling. In the present work, the concrete and reinforcement components are created separately using ABAQUS software. The cell type of the concrete finite element model for the shear wall and foundation base is an eight-node solid unit (C3D8R), while the cell type of the finite element model for the longitudinal reinforcement, tie bars, and hoop bars is a three-dimensional solid unit (T3D2) [36].

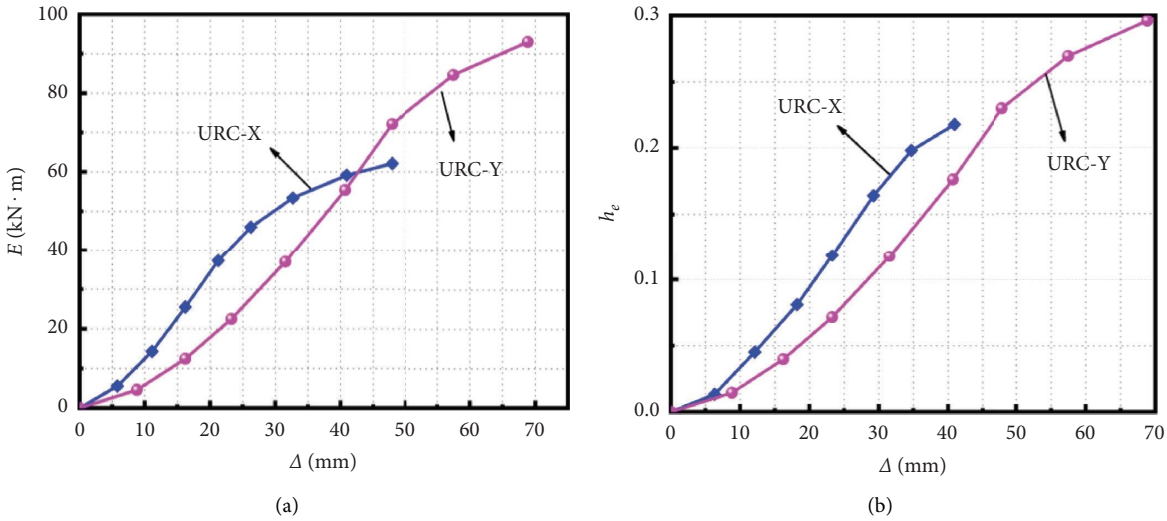

Figure 19: Energy dissipation capacity.

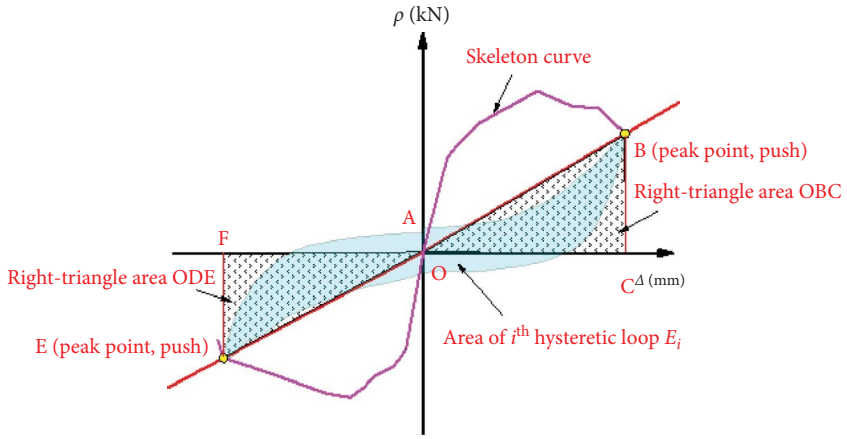

Figure 20: Calculation chart of energy dissipation coefficient.

In order to more realistically reflect the interaction between the reinforcement and the concrete, the concrete possesses the same nodes as the reinforcement (the strain of the reinforcement coincides with the strain of the concrete units) [37]. The interaction between the reinforcement and the concrete is chosen to be "embedded," in which the concrete has the same nodes for each reinforcements. In terms of contact, considering the friction slip between steel bars and core concrete, the interface between steel bars and concrete is defined as "face-to-face contact." The normal behavior adopts the "hard contact" and "penalty" functions, while the friction coefficient is set to 0.6 [38, 39].

A steel cushion with high stiffness is set at the top of the column as a loading plate so that the top of the column can be uniformly stressed to prevent stress concentration. The constraint of the base bottom support is set to Ux = Uy = Uz = 0, and the ABAQUS coupling command is used to connect the set reference point RP-1 with the steel cushion.

The model loading method adopts two loading steps. In the first analysis step, the axial force of 100 kN was applied to the top of the column. The increment step was initially 0.001, while the maximum was 0.01, which continued to the latter analysis step. In the second analysis, the horizontal displacement load is applied. The loading method is a mixed force-displacement control, with force control before the bar yields and displacement control after the bar yields, with two reciprocal cycles.

We conducted a parametric study on the mesh convergence and obtained the optimal finite element mesh of 50 mm with a short computation time and relatively accurate results. The finite element model is shown in Figure 21.

5.2. Material Constitutive Mode

5.2.1. Concrete Principal Structure Model. The concrete damage plasticity (CDP) model can effectively simulate the changes of concrete structures under cyclic reciprocal

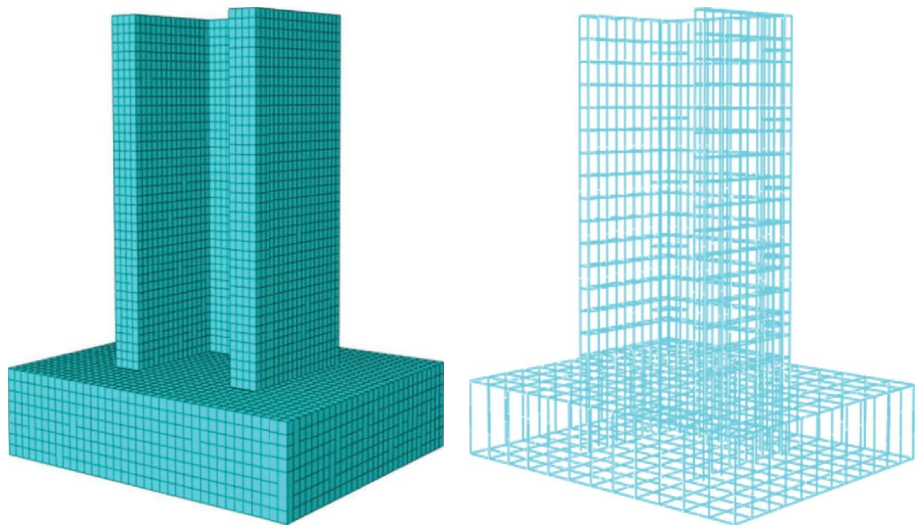

(a) (b)

Figure 21: Finite element model. (a) Concrete. (b) Reinforced steel skeleton.

loading. Thus, the inelastic behavior of concrete is defined by the CDP model, which considers isotropic damage elasticity as having isotropic tensile and compressive plasticity and takes into account the degradation of elastic stiffness due to plastic strain during tensile and compressive processes [40, 41]. Defining the damage plastic model in ABAQUS requires the uniaxial compression and tensile behavior of concrete. For the stress-strain relationship of concrete under uniaxial compression, the Chinese specification (GB 50010-2010) [2] is adopted, as shown in Figure 22. The expression is given as follows:

$$\sigma_c = \frac{n\left(\varepsilon/\varepsilon_{cr}\right)}{n - 1 + \left(\varepsilon/\varepsilon_{cr}\right)^n} f_{cr}, \qquad n = \frac{E_c \varepsilon_{cr}}{E_c \varepsilon_{cr} - f_{cr}}, \tag{3}$$

where f_{cr} is the representative value of the uniaxial compressive strength of concrete; ε_{cr} is the corresponding compressive strain; and E_c is the elastic modulus of concrete. d_C is the uniaxial compressive damage evolution parameter defined in the CDP model.

The stress-strain relationship of concrete under tensile state is assumed to be linear elastic until the tensile strength is reached. In this study, considering the strain softening behavior of cracked concrete, the stress-strain relationship after failure in the Chinese specification (GB 50010-2010) [2] is used to represent. One out of 10 of the cracking strain is the failure tensile strain. The concrete compression and tensile damage parameters defined in the material model are shown in Figure 23.

5.2.2. Reinforcing Steel Principal Structure Model. Steel bars conform to the typical characteristics of elastic and plastic materials and, therefore, have well-defined intrinsic structure relationships in finite element analysis, and a bilinear follower strengthening model was used for steel bars in this simulation. The model achieved good results in simulating the member performance under the proposed static loads [42, 42].

5.3. Numerical Simulation Results

5.3.1. Concrete Damage Distribution. The distribution of compressive damage (DEMAGEC) and tensile damage (DEMAGET) for each member at ultimate bearing capacity is shown in Figures 24 and 25.

(1) Component URC-X Damage Distribution Cloud Analysis. As can be seen from the URC-X compression and tensile damage distribution clouds for the members are shown in Figure 24.

(1) DEMAGEC mainly responds to the compression of the shear wall in the simulation process. s can be seen from Figure 25, the compression damage is mainly concentrated atr the junction of the wall limb and web of the web member and the end of the wall limb, which is comparable to the actual test where the concrete is crushed, and the maximum compression damage is up to 0.76. DEMAGET mainly responds to the tension of the shear wall specimen in the simulation process and the crack DEMAGET mainly responds to the tensile condition of the shear wall specimens during the simulation and the development of cracks.

(2) Through the contour figure as well as observing the whole model loading process, both compression damage and tensile damage appear at the edge of the lower corner of the wall limb at the earliest and appear earlier. A transverse red line appears at the intersection of the base and shear wall on the

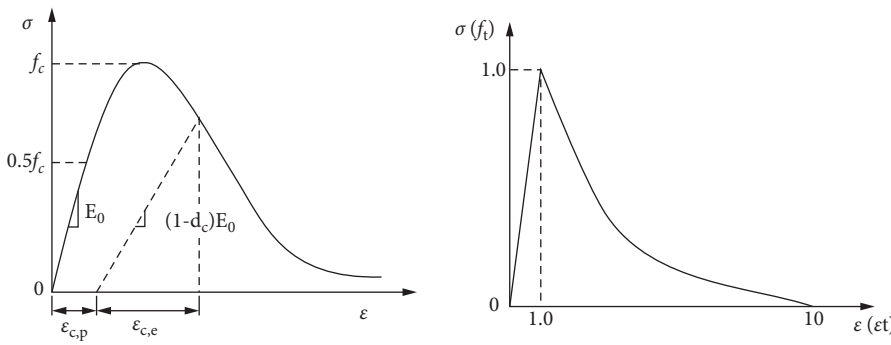

Figure 22: Concrete damage plasticity models compressive and tensile stress-strain relationships.

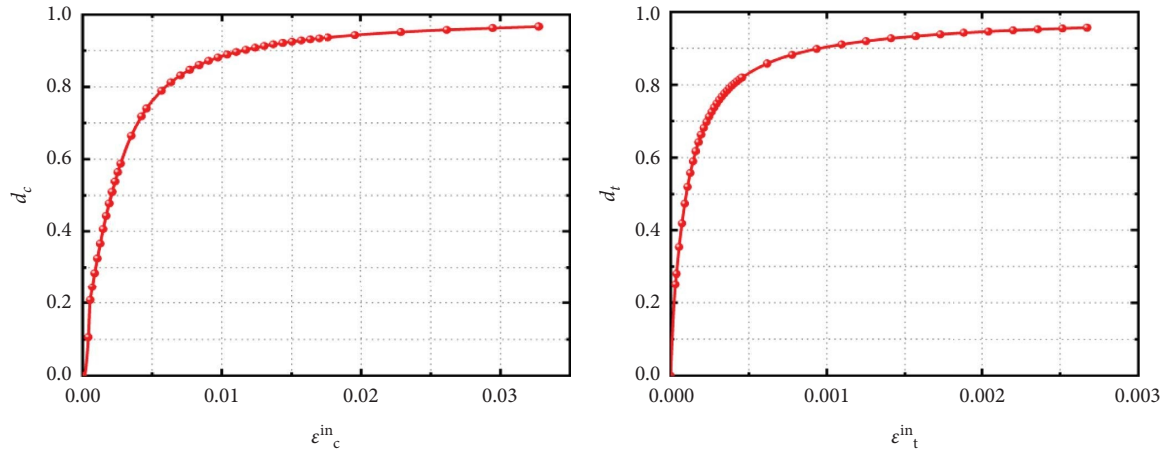

Figure 23: Compressive and tensile damage behaviors of concrete.

compressive damage map, representing the development of cracks. With the loading of displacement, multiple transverse cracks appeared above the first transverse crack, and the damage of the transverse cracks below continued to increase, representing the gradual widening of the cracks, and finally all the transverse cracks were stepped, and the transverse cracks at the end of the wall limb developed into oblique cracks in a 45° oblique direction. As the displacement increases, the damage continues to accumulate; transverse cracks appear to be 1/2 of the wall no longer appear upward, but the transverse cracks widen as does the development of oblique cracks; at this time, the wall's early batch crack damage reached 0.675. After this period, the cracks no longer appear, but only the deepening of the original crack color, representing the spread of the original cracks, until more than 1/2 of the wall is all red and more than 1/2 appears obvious to be 45° cross-diagonal cracks with a maximum of 0.736.

(3) The first crack damaged by tension first appeared at the junction of web and wall limb. With the increase of displacement, a large number of transverse cracks appeared in the wall, and part of the transverse cracks developed into oblique cracks, which extended from the junction to the upper part of 45° to the end of the wall. We can obviously see from the figure that the damage value below the oblique crack (the lower part of the wall) was very large. It indicates that the shear wall has been damaged obviously.

(2) Component URC-Y Damage Distribution Cloud Analysis. From the URC-Y compression and tensile damage distribution clouds of the members shown in Figure 25, it can be seen that:

(1) Through the damage clouds of the two specimens, it is obvious that the damaged area of the two specimens is symmetric, which completely eliminates the influence of the objective factors of the test.

(2) The DANAGEC and DAMAGET animation analyses show that there is no change in the specimen at the beginning of loading, and the earliest damage, whether in compression or tension, appears at the edge of the lower corner of the wall limb, and with displacement loading, the earliest crack appears, extending to the web to form a through the crack. Then, alternating transverse cracks appeared in the upper part of the member, which gradually developed in the direction of 45° diagonally downward and gradually formed 45° through diagonal cracks.

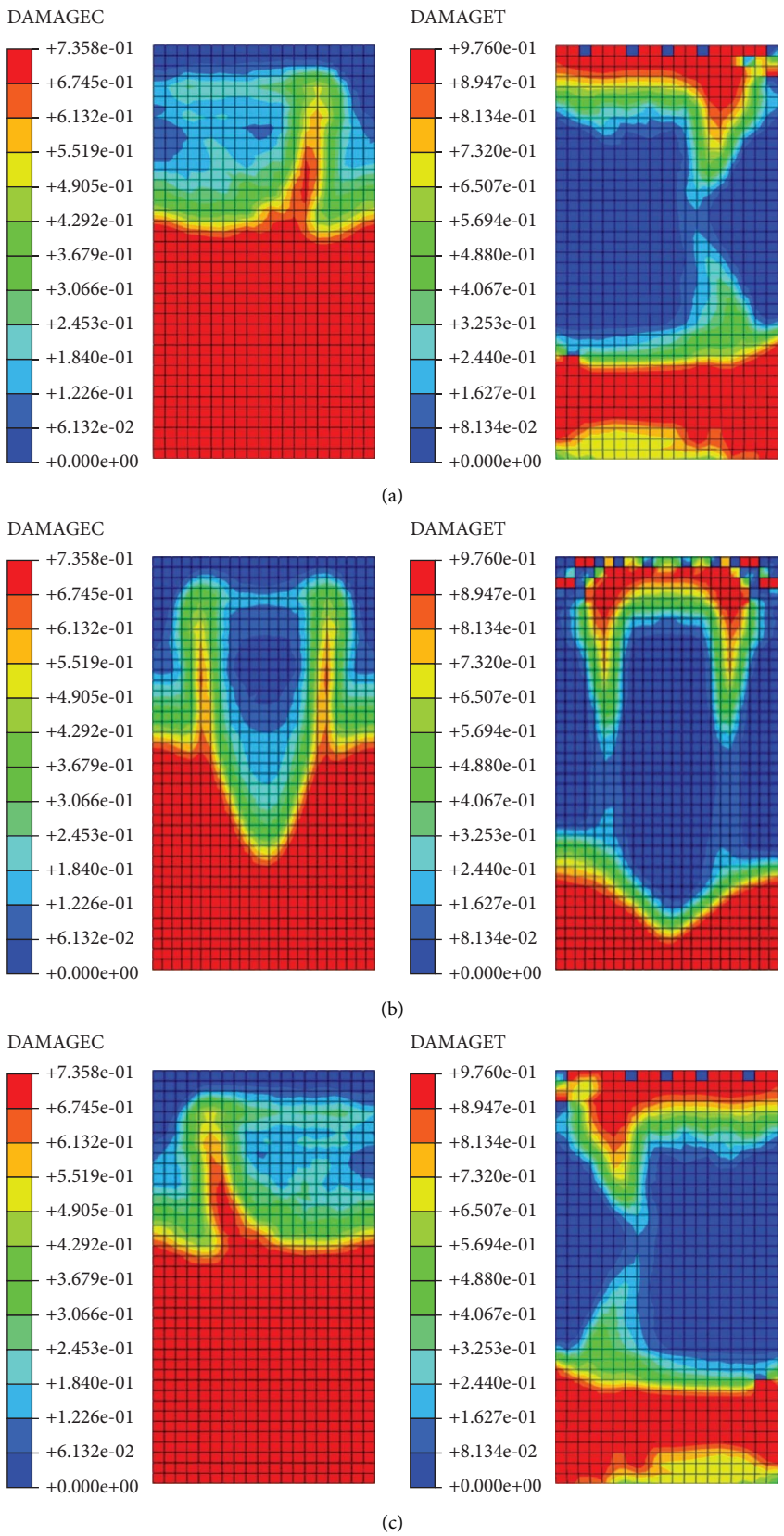

Figure 24: URC-X compression and tensile damage distribution clouds of the member. (a) Wall limb 1 compression and tensile damage distribution clouds. (b) Web compression and tensile damage distribution clouds. (c) Wall limb 2 compression and tensile damage distribution clouds.

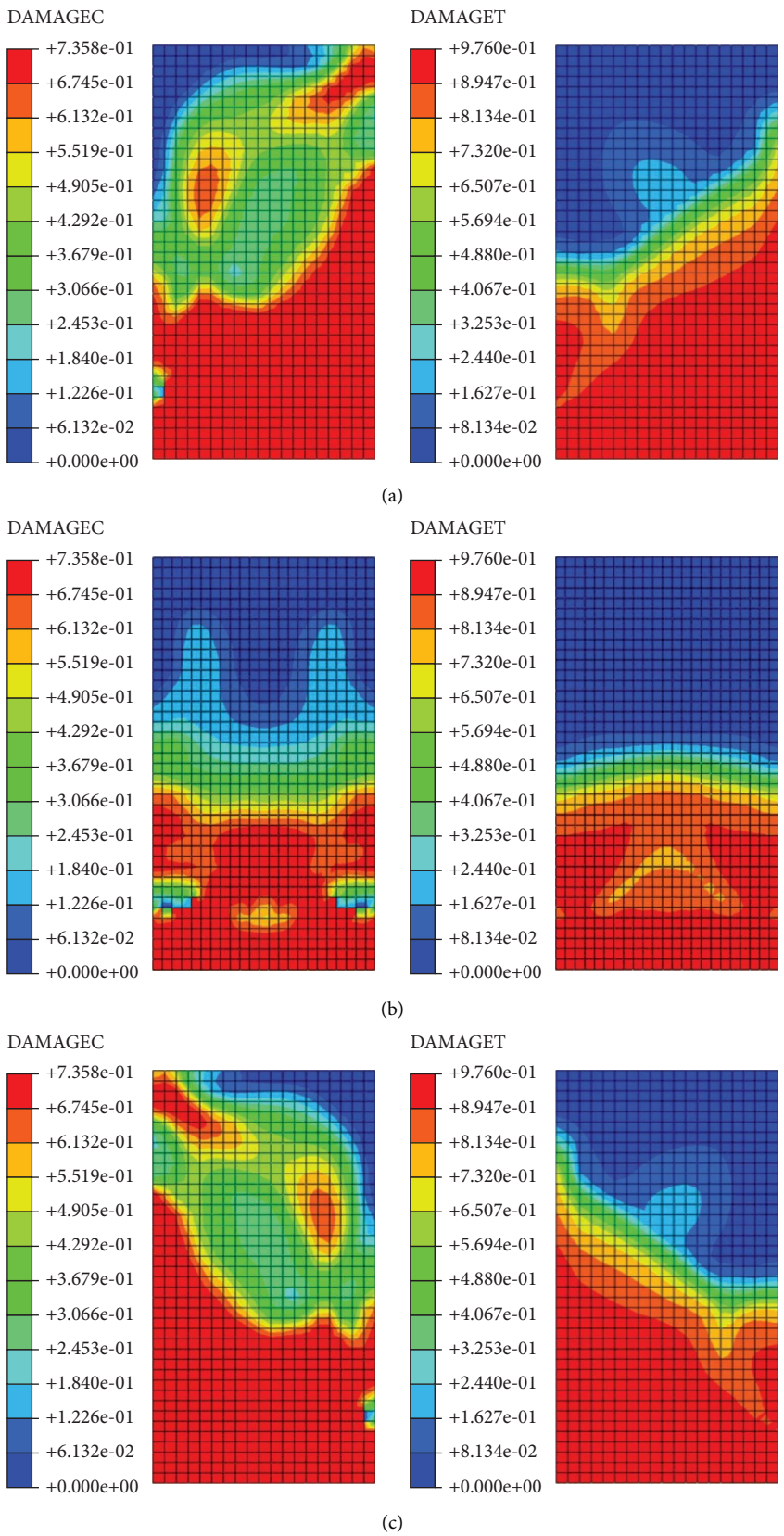

Figure 25: URC-Y compression and tensile damage distribution clouds of the member. (a) Wall limb 1 compression and tensile damage distribution clouds. (b) Web compression and tensile damage distribution clouds. (c) Wall limb 2 compression and tensile damage distribution clouds.

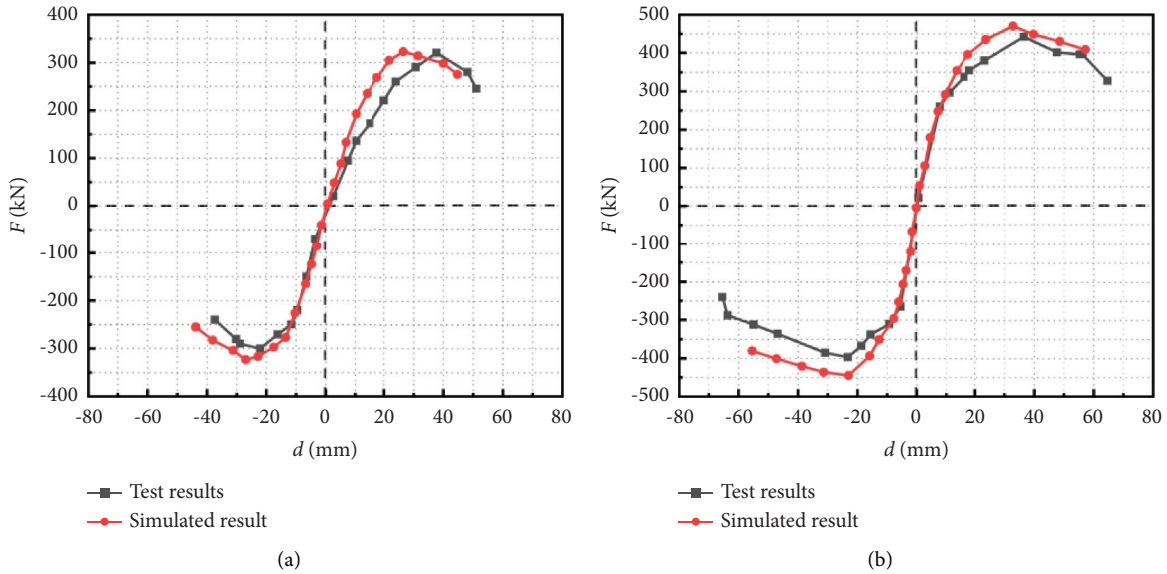

Figure 26: Comparison of simulation and test skeleton curves. (a) URC-1. (b) URC-2.

Table 6: Comparison of the finite element analysis value and test value of each load point.

Specimen number	Methods	Δ_y (mm)	P_{max} (kN)	Δ_{max} (mm)	Δ_u (mm)
URC-X	Test	20.04	340.12	37.82	48.37
	Simulation	17.52	342.56	31.47	44.79
URC-Y	Test	19.19	458.16	36.56	64.56
	Simulation	18.75	464.92	32.88	57.18

At the later stage of loading, the new cracks are fewer, and the original cracks extend upward and form 45° through-slope cracks with the web, with the maximum damage reaching 0.976.

(3) The wall damage below 1/2 is a serious damage area, and the above 1/2 part forms 45° oblique cracks. An obvious bulging phenomenon can be found in the lower part of the wall, which is also a concrete crushing area in the actual test.

5.3.2. Comparison of Numerical Simulation Results with Experimental Results. Figure 26 shows the comparison of the envelope diagram between the specimen results and the finite element results. The figure shows that the test data agree well with the finite element results. To compare the results of the experiments and numerical simulations intuitively, the characteristic point values of the skeleton curves are shown in Table 6. The results are as follows:

(1) The load-displacement skeleton curve obtained by finite element simulation is consistent with the test results. The error between the simulation results of peak load and the test results is 0.72% and 14.7%. The relative error is less than 15%. The ABAQUS software can effectively simulate the behavior of reinforced concrete *U*-shaped section walls under cyclic loading.

(2) The yield load, peak load, and ultimate load obtained by numerical simulation are all smaller than the corresponding test results. The error analysis is as follows:

① Interaction between reinforcement and concrete was observed. In the actual test, the interaction between the steel bar and concrete has a bond-slip section. In finite element modeling, the combination of steel and concrete is directly embedded, while the combination is ideal, which may affect the results.

② The constitutive relationship of materials is not exactly the same. Although the constitutive relationship of the reinforced concrete used in the modeling process matched the test, concrete is an ideal homogeneous material in ABAQUS. Due to the artificial vibration in the actual pouring process, the specimen is not a homogeneous material, resulting in a large difference between the stress of the specimen in the test process and that of the finite element model.

③ Accidental error during the test. In addition to manual vibration, mix proportion, template accuracy, and other factors will also produce errors in the process of specimen production. Factors such as load application efficiency, data measurement, and calculation accuracy may cause final errors.

6. Conclusion

In the current work, the seismic performance of the *U*-shaped cross-section shear wall under cyclic loading was both tested and numerically studied. The seismic performance of the *U*-shaped shear wall under horizontal load in two directions was obtained. On this basis, the seismic performance mechanism of the *U*-shaped section wall was analyzed and compared with the static and cyclic test results of other short-leg shear walls with various sections. The following conclusions are reached:

(1) Both the test and simulation results show that this section type of wall can withstand large bending moments and shear forces in both directions, but the specimen URC-Y has better ductility, greater cumulative dissipated energy, and more stable resistance to lateral forces. The bearing capacity of the *U*-shaped section shear wall on the strong axis (O ⟶ D ⟶ C ⟶ O) is 34.71% higher than that on the weak axis (O ⟶ A ⟶ B ⟶ O), while the ductility increases by 39.42%.

(2) The test and simulation results show that both specimen URC-X and specimen URC-Y can meet the seismic safety requirements of the project. In order to take advantage of the seismic performance of the *U*-shaped section shear wall, it is recommended that the strong axis of the *U*-shaped section shear wall be arranged parallel to the direction of the larger forces on the building. In addition, the *U*-shaped section shear wall, as the ground floor part of the actual project, has a large damaged area concentrated in the web and the bottom end of the wall limbs, which should be designed and constructed in accordance with the key strengthening elements in the project.

(3) By comparing and analyzing rectangular, *T*-shaped, and *L*-shaped section shear walls, the bearing capacity performance, ductility, and lateral displacement resistance of *U*-shaped section shear walls have obvious advantages under the same conditions. It is therefore suggested that multiple shear wall elements can be arranged to form a *U*-shaped section in the actual project.

(4) The numerical simulation results are in good agreement with the experimental data, indicating that the nonlinear model established by this numerical analysis can better simulate the damage mechanism and mechanical properties of *U*-shaped section shear walls, which provides an effective research method for relevant scientific research in the field of civil engineering.

(5) In order to better understand the seismic performance of *U*-shaped section shear wall structures, it is proposed to further analyze the study of simultaneous two-way double-cycle loading of *U*-shaped section walls along two major axis directions in the future.

Data Availability

Data are available upon request from the authors.

Conflicts of Interest

The authors declare that they have no conflicts of interest.

Acknowledgments

This study was supported by the Jilin Province Natural Fund Project: 20200201227JC.

References

[1] P. Zhou, *Study on Seismic Performance of Short-Leg Shear wall with Different Section forms[D]*, Northwest agriculture and forestry university, Xianyang, China, 2019, in chinese.

[2] N. Lu, *Study on Seismic Performance of Short-Leg Shear wall Joints [D]*, Hunan university of technology, Hunan, China, 2016, in chinese.

[3] Q. Z. Ban, "Infiluence of shear wall layout on structural performance of irregular high-rise flats [J]," *Journal of Building Structures*, vol. 48, no. s2, pp. 98–101, 2018, in chinese.

[4] B. S. Rong, "Short-shear wall structure system in High-rise building [J]," *Jounal of buliding structures*, no. 06, pp. 14–19, 1997, in chinese.

[5] X. Wang, Y. Su, and L. Yan, "Experimental and numerical study on steel reinforced high-strength concrete short-leg shear walls," *Journal of Constructional Steel Research*, vol. 101, no. oct, pp. 242–253, 2014.

[6] F. Naeim, M. Lew, L. D. Carpenter et al., "Performance of tall buildings in Santiago, Chile during the 27 February 2010 offshore Maule, Chile earthquake[J]," *The Structural Design of Tall and Special Buildings*, wiley, Hoboken, New Jersey, US, 2010.

[7] A. A. Behrouzi, A. W. Mock, D. E. Lehman, L. N. Lowes, and D. A. Kuchma, "Impact of bi-directional loading on the seismic performance of C-shaped piers of core walls[J]," *Engineering Structures*, vol. 225, 2020.

[8] K. Beyer, A. Dazio, and M. J. N. Priestley, "Quasi-static cyclic tests of two U-shaped reinforced concrete walls," *Journal of Earthquake Engineering*, vol. 12, no. 7, pp. 1023–1053, 2008.

[9] R. Constantin and K. Beyer, "Behaviour of U-shaped RC walls under quasi-static cyclic diagonal loading," *Engineering Structures*, vol. 106, no. 1, pp. 36–52, 2016.

[10] N. Ile and J. M. Reynouard, "Behaviour of U-shaped walls subjected to unlaxial and blaxial cyclic lateral loading[J]," *Journal of Earthquake Engineering*, vol. 9, no. 1, pp. 67–94, 2005.

[11] Gb 50011-2010, *Seismic Design Code of Building*, china buliding industry press, Beijing, China, 2011, in chinese.

[12] Z. X. Li, *Theory and Technology of Engineering Structure Test*, University of Tianjin Press, Tianjin, China, 2004.

[13] H. Gao, *Discussion of Several Problems in PKPM Software in Modeling*, China Academy of Building Science, Nationwide, China, 2006.

[14] Gb 50010-2010, *Design Code for concrete Structure*, china building industry press, Beijing, China, 2010, in chinese.

[15] Gj3-2010, *Technical Specification for concrete Structures of High-Rise Building*, china building industry press, Beijing, China, 2010, in chinese.

[16] Jgj 149-2017, *Technical Specification for concrete Special-Shaped Column Srtucture*, china building industry press, Beijing, China, 2017, in chinese.
[17] Gb/T 50081-2002, *Standard Method for Mechanical Properties of Ordinary concrete*, china building industry press, Beijing, China, 2002, in chinese.
[18] Gb/T 50152-201, *Standard Test Method for concrete Structure*, china building industry press, Beijing, China, 2012, in chinese.
[19] Gb/T 228-2010, *Standard of Room Temperature Test Method for Tensile Test of Metal Materials*, China Building Industry Press, Beijing, China, 2010, in chinese.
[20] Gb 1499.2-2007, *Steel for Reinforced concrete Part 2: Hot Rolled Ribbed Bar*, China Building Industry Press, Beijing, China, 2007, in chinese.
[21] Gb 50204-2002, *Code for Acceptance of Constructional of concrete Structure*, China Building Industry Press, Beijing, China, 2002, in chinese.
[22] J. Zhao, G. Cai, A. Si Larbi et al., "Hysteretic behaviour of steel fibre RC coupled shear walls under cyclic loads: experimental study and modelling," *Engineering Structures*, vol. 156, no. 1, pp. 92–104, 2018.
[23] X. Zhai, J. Yan, and C. Cao, "Seismic performance and flexible connection optimization of prefabricated integrated short-leg shear wall filled with ceramsite concrete," *Construction and Building Materials*, vol. 311, 2021.
[24] J. T. Yu, W. L. Xu, J. H. Lin et al., "Mechanism analysis of pinching effect of reinforced concrete columnbased on extendedfinite element method[J]," *Engineering Mechanics Press*, vol. 32, no. 11, p. 10, 2015.
[25] P. L. Zhang, *Experimental Study on Sesmic Behavior and Damage Analusis of Short-Leg Shear wall[D]*, Xi'an University of architecture and trchnology, Xi'an, China, 2011.
[26] R. Park, "Evaluation of ductility of structures and structural assemblages from laboratory testing = Evaluation de la ductilité de structures et de liaisons à partir d'essais en laboratoire[J]," *Bulletin of the New Zealand National Society for Earthquake Engineering*, New Zealand Society for Earthquake Engineering, Wellington, New Zealand, 1989.
[27] A. Sx, A. Zw, A. Xl et al., "Study of effects of sleeve grouting defects on the seismic performance of precast concrete shear walls[J]," *Engineering Structures*, vol. 236, 2021.
[28] J. Li, Z. Wang, F. Li, B. Mou, and T. Wang, "Experimental and numerical study on the seismic performance of an L-shapeddouble-steel plate composite shear wall," *Journal of Building Engineering*, vol. 49, 2022.
[29] Jgj 101-2015, *Test Specification for Anti-seismic Construction*, china building industry press, Beijing, Chine, 2015, in chinese.
[30] J. B. Yan, H. T. Hu, and T. Wa Ng, "Cyclic tests on concrete-filled composite plate shear walls with enhanced C-channels," *Journal of Constructional Steel Research*, vol. 179, Article ID 106522, 2021.
[31] A. S. Genikomsou and M. A. Polak, "Finite element analysis of punching shear of concrete slabs using damaged plasticity model in ABAQUS," *Engineering Structures*, vol. 98, no. 1, pp. 38–48, 2015.
[32] B. Zhuang, *The Finite Element Analysis and Application Based on ABAQUS [M]*, Qinghua University Press, Beijing, China, 2009.
[33] W. Xiaoqiang, W. Jifeng, W. Zhenqing, L. Wenyan, and Z. Limin, "Finite element simulation of the failure process of single fiber composites considering interface properties[J]," *Composites Part B: Engineering*, vol. 45, 2013.
[34] A. Xu, T. Vodenitcharova, K. Kabir, E. Flores-Johnson, and M Hoffman, "Finite element analysis of indentation of aluminium foam and sandwich panels with aluminium foam core," *Materials Science and Engineering: A*, vol. 599, no. APR.2, pp. 125–133, 2014.
[35] *ABAQUS Analysis User's Manual 6.10-EF*, Dassault Systems Simulia Corp, Providence, RI, USA, 2010.
[36] Y. T. Wu, D. Y. Kang, and Y. B. Yang, "Seismic performance of steel and concrete composite shear walls with embedded steel truss for use in high-rise buildings," *Engineering Structures*, vol. 125, no. 15, pp. 39–53, 2016.
[37] L. H. Han, G. H. Yao, and Z. Tao, "Performance of concrete-filledthin-walled steel tubes under pure torsion," *Thin-Walled Structures*, vol. 45, no. 1, pp. 24–36, 2007.
[38] B. G. Rabbat and H. G. Russell, "Friction coefficient of steel on concrete or grout," *Journal of Structural Engineering*, vol. 111, no. 3, pp. 505–515, 1985.
[39] S. H. Lee, A. Abolmaali, K. J. Shin, and H. D Lee, "ABAQUS modeling for post-tensioned reinforced concrete beams," *Journal of Building Engineering*, vol. 30, Article ID 101273, 2020.
[40] M. Talaat, E. Yehia, S. A. Mazek, M. M. Genidi, and A. G Sherif, "Finite element analysis of RC buildings subjected to blast loading," *Ain Shams Engineering Journal*, vol. 13, no. 4, Article ID 101689, 2022.
[41] I. M. Alshaikh, B. A. Bakar, E. A. Alwesabi, A. M. Zeyad, and H. M. Magbool, "Finite element analysis and experimental validation of progressive collapse of reinforced rubberized concrete frame," *Structures*, vol. 33, pp. 2361–2373, 2021.
[42] A. Raza, B. Masood, and I. Hussain, "Finite element modelling and theoretical predictions of FRP-reinforced concrete columns confined with various FRP-tubes[J]," *Structures*, vol. 26, 2020.